Online low-light sand-dust video enhancement using adaptive dynamic brightness correction and a rolling guidance filter

Dongdong Ni, Zhenhong Jia *, Jie Yang *member, IEEE,* and Nikola Kasabov, *Fellow, IEEE*

***Abstract*—Sand-dust videos obtained in a low-light environment are characterized by low contrast, nonuniform illumination, color cast, and considerable noise. To realize sand-dust removal and brightness enhancement simultaneously, this paper proposes an online low-light sand-dust video enhancement method using adaptive dynamic brightness correction and a rolling guidance filter. The proposed dual-threshold interframe detection strategy involves two methods to treat low-light sand-dust video frames. The first method involves two components: an adaptive dynamic brightness correction algorithm to correct the color deviation of the low-light video frame and improve its brightness and a rolling guidance filter combined with guided image filtering to enhance the frame details. The second method enhances the quality of the incoming frame by reducing the amount of calculation. The first frame of the video is processed using the first method. The processing method of each subsequent frame is determined according to its interframe detection value with the buffer frame. Through qualitative and quantitative comprehensive experiments on low-light sand-dust images and videos, the performance of the proposed method is compared with those of state-of-the-art methods. The proposed method for frame quality improvement achieves the best visual effect in enhancing the quality of low-light sand-dust images, as indicated by the best objective evaluation indicators. Moreover, compared with the framewise enhancement method, the video processing efficiency associated with the dual-threshold interframe detection strategy is 2.77 times higher.**

***Index Terms*—Low-light sand-dust video, adaptive dynamic brightness correction, rolling guidance filter, dual-threshold interframe detection strategy.**

I. Introduction

HUMAN beings obtain most of their information using the visual system, in the form of images. Thus, images are irreplaceable information carriers for human perception [1]. However, images and videos captured in outdoor scenes are often degraded by the interaction of atmospheric phenomena, which affects people's access to correct and effective information [2]. In sand-dust weather, the sand-dust particles suspended in the air absorb, emit, or scatter light, thereby severely degrading the videos and images collected by visual acquisition equipment. These videos and images suffer from color cast, reduced contrast, noise, and loss of details, which impede important computer vision tasks, such as target recognition [3], road monitoring [4], aerospace applications [5], military surveys [6], and satellite remote-sensing monitoring [7]. Therefore, removing the effect of sand dust from videos and images collected under sand-dust weather and recovering the scene correctly are essential and fundamental steps in computer vision. In addition, with the dramatically increasing number of surveillance cameras installed worldwide, real video is available to be streamed online. Thus, an online scheme must be established to enhance low-light sand-dust videos: Such a scheme must be able to manage the incoming data of each frame online without storing the complete video in memory.

Many researchers have attempted to address these issues [8]-[20]. Although most of the existing image methods are effective for daytime sand-dust removal, their performance is inadequate for low-light sand-dust removal due to the multiple light scattering and low level of illumination. Thus, low-light image sand-dust removal continues to be a challenging task. In general, daytime illumination is dominated by uniformly distributed sunlight, whereas the illumination in a low-light environment is spatially irregular and susceptible to noise [21]. Moreover, the illumination is extremely weak, the visibility is reduced, and the scene details are hidden, resulting in the failure of the currently used priors and assumptions, such as the color attenuation [22] and dark channel priors [23]. Although various effective methods for low-light image enhancement have been developed [20], [24]-[27], [29], sand-dust removal and brightening are treated separately in low-light image processing. Consequently, the ambient illumination is dim in images treated for sand-dust removal, and sand dust remains in images treated for low light. Considering these aspects, this paper proposes an online low-light sand-dust video enhancement method using adaptive dynamic brightness correction and a rolling guidance filter to simultaneously realize sand-dust removal and brightness enhancement.

In our preliminary work [28], we developed a straightforward and unsupervised method for improving sand-dust video quality. This practical and efficient method is effective in daytime conditions but fails in low-light conditions. To solve the problem of dimness and noise in the existing method [28] when processing low-light sand-dust videos and images, we design an adaptive dynamic brightness correction (ADBC) algorithm and a rolling guidance filter combined with a guided image filtering (RGF-GIF) algorithm. The ADBC algorithm enhances the brightness of low-light sand-dust videos, and

Dongdong Ni and Zhenhong Jia are with the College of Information Science and Engineering, Xinjiang University, Urumqi 830046, China. (Corresponding author: Zhenhong Jia, email: jzhh@xju.edu.cn)

Jie Yang is with the Institute of Image Processing and Pattern Recognition, Shanghai Jiao Tong University, Shanghai 200400, China. (email:jieyang@sjtu.edu.cn)

Nikola Kasabov is with Knowledge Engineering and Discovery Research Institute, Auckland University of Technology, Auckland 1020, New Zealand. (email:nkasabov@aut.ac.nz)

the RGF-GIF algorithm enhances the details of the low-light sand-dust videos and suppresses noise. In addition, the dual-threshold interframe detection strategy designed in this study can reduce the time for calculating intermediate variables compared with the interframe detection strategy.

Fig. 1 illustrates the process flow of the proposed method. First, the dual-threshold interframe detection strategy initializes the buffer frame as the first frame of the low-light sand-dust video. Second, the ADBC and RGF-GIF algorithms are used for color correction, brightness correction, and detail enhancement. Additionally, the frame variation is initialized as the difference between the processing result of the first frame and buffer frame at each position of the R, G, and B color channels, and the intermediate variables in the frame image enhancement process are saved. Finally, the dual-threshold interframe detection strategy provides two optional methods to improve the quality of each subsequent frame. The first method uses the ADBC and RGF-GIF algorithms to process the incoming frame. At the same time, the buffer frame is updated to the incoming frame, the frame variation is updated to the difference between the incoming frame and processed incoming frame, and the new intermediate variables are saved. The second method enhances the quality of the incoming frame by reducing the amount of calculation. The threshold T_h is a critical value that determines which method is used to process the incoming frame. SV represents the interframe detection value of the incoming and buffer frames. If $SV < T_h$, the first method is used to process the incoming frame; otherwise, the second method is used to process the incoming frame. The second method adopts two strategies to reduce the amount of computation. If $SV \geq T_f$, the sum of tonal values of the incoming frame and frame variation at each position of the R, G, and B color channels are considered the processing result of the incoming frame. If $SV < T_f$, the intermediate variables are directly substituted into Equations (1), (2), (6), and (16) to obtain the result of the incoming frame to reduce the time for calculating the intermediate variables. Furthermore, the buffer frame is updated to the incoming frame, and the frame variation is updated to the difference between the incoming frame and processed incoming frame.

The contributions of this research can be summarized as follows:

1. An adaptive dynamic brightness correction algorithm based on the average brightness information of the frame is proposed, which can dynamically adjust the brightness range of the frame combined with the brightness information characteristics of the frame.

2. A rolling guidance filter algorithm combined with guided image filtering is developed to enhance the details of the frame and suppress the influence of noise on the enhancement process.

3. A dual-threshold interframe detection strategy is designed to improve the efficiency of processing low-light sand-dust videos without deteriorating the processing effect.

The remaining paper is organized as follows. Section II provides a review of the related work. Section III describes the principles and process flow of the proposed method. Section IV presents the experimental results. Section V presents the concluding remarks.

II. Related work

Clear scenes satisfy human visual needs and are beneficial for higher-level processing. This section provides a brief review of the existing work focused on low-light and sand-dust image enhancement.

Low-light enhancement methods for a single image have recently attracted significant research attention. For example, Wu et al. [24] proposed an HE-based method that adaptively controls the contrast gain according to the potential visual importance of the intensities and pixels to guarantee global contrast preservation. Li et al. [20] used a robust Retinex model to improve the brightness of dusty images. Dong et al. [25] exploited a DCP-based method to improve the brightness of low-light videos. Lei et al. [29] proposed a simple yet effective low-light image enhancement method to perceive unknown information from dark areas. However, traditional methods cannot effectively extract enhanced details and encounter challenges related to low contrast and unnatural colors. Learning-based methods have achieved considerable success in low-light image enhancement. Xu et al. [26] proposed a novel frequency-based image decomposition-and-enhancement model to adaptively enhance the image contents and details in different frequency layers while suppressing noise. Wang et al. [27] proposed a novel framework for low-light image enhancement based on a normalizing flow model, which can effectively adjust illumination and suppress noise and artifacts. Liu et al. [34] systematically reviewed and evaluated the existing single-image low-light enhancement algorithms.

In recent years, with the increasing frequency of sand-dust weather, video and image clarity processing under sand-dust weather has received extensive attention. The methods for enhancing sand-dust videos and images can be divided into three categories: image enhancement methods, image restoration methods, and deep-learning methods.

Image enhancement methods enhance images according to the image degradation characteristics, independent of the imaging process of objects in the image environment. Representative algorithms include histogram equalization techniques and multiscale Retinex enhancement algorithms with color recovery [30], [31]. For example, Shi et al. [8] developed a normalized gamma transformation-improved CLAHE method for enhancing the image contrast, which uses the normalized gamma function to reduce the excessive increase in the brightness induced by CLAHE. Park et al. [9] proposed an efficient sand-dust image enhancement algorithm using a successive color balance to obtain a coincident chromatic histogram. Li et al. [10] proposed a region-adaptive image dehazing and enhancement method based on a replaceable plug-in region segmentation module and seamless stitching for hazy outdoor scenes with a large range of depth of field. The most notable advantage of such methods is that the prior conditions of the images do not need to be considered, resulting in high calculation efficiency. However, in practical applications, computer-vision-acquisition equipment is often contaminated with noise [32]. Thus, in addition to enhancing

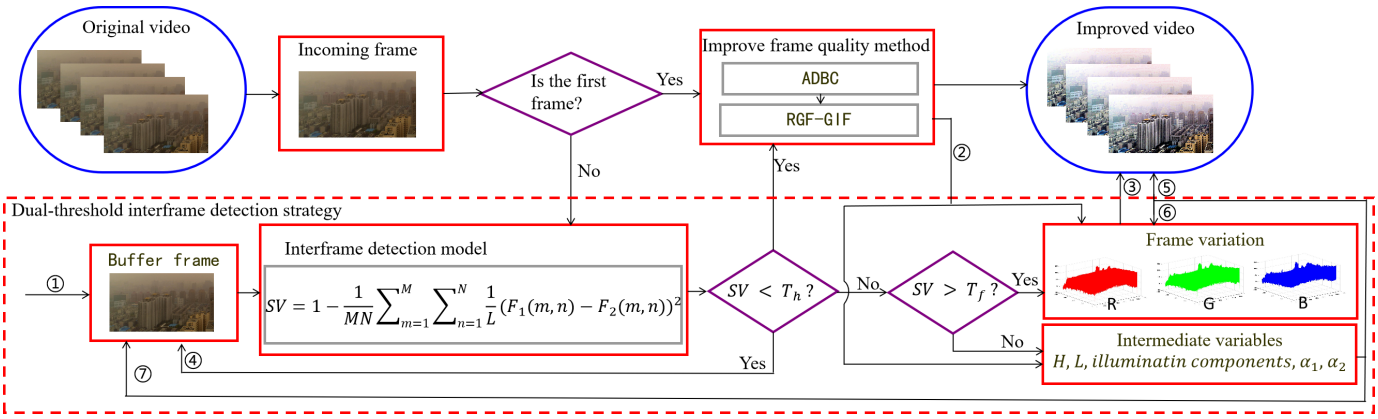

Fig. 1. Process flow of the proposed method. In step ①, the buffer frame is initialized to the first frame of the video to be processed. In steps ② and ⑥, the frame variation is updated to the difference between the processed frame and buffer frame at each position of the R, G, and B color channels, and the intermediate variables in the image enhancement process are saved. In step ③, the sum of tonal values of the incoming frame and frame variation at each position of the R, G, and B color channels is set as the processing result of the incoming frame. In steps ④ and ⑦, the buffer frame is updated to the incoming frame. In step ⑤, the intermediate variables are directly substituted into Equations (1), (2), (6), and (16) to obtain the result of the incoming frame to reduce the time for calculating the intermediate variables.

the visual effect of images, such methods also amplify the noise, thereby deteriorating the video and image quality. As shown in Figs. 9(d), 9(f), 15(b), and 15(g), although the license plate information is enhanced, the noise is also amplified.

Image restoration methods construct a corresponding physical model by analyzing the reasons for image degradation and restore the original information of the image in combination with prior knowledge. The most widely used method, proposed by He et al. [33], adopts the dark channel prior for haze removal. Inspired by this method, Gao et al. [11] reversed the blue channel and used the dark channel prior to estimate the atmospheric light and transmission map to recover sand-dust images. Yang et al. [12] applied optical compensation and Gaussian adaptive transmission to eliminate the color cast of hazy dust images and enhance their visibility. Salazar et al. [13] developed a morphological reconstruction method based on the dark channel prior to eliminate the effect of dust. Shi et al. [14] used a halo-reduced DCP dehazing method and gamma function to obtain normal visual colors and a detailed clear image. Such methods can obtain promising experimental results for data that meet the prior conditions; however, they are ineffective for data that do not meet the prior conditions.

Deep-learning methods typically apply two strategies to enhance sand-dust images and videos. The first strategy is to estimate the transmittance and atmospheric light in the atmospheric scattering model through deep learning [16], [17]. The second strategy is to establish an end-to-end network from sand-dust images to sand-dust-free images through deep learning [15], [18], [19]. Notably, the construction of a network to improve the definition of dust images based on deep learning is a data-driven method that requires comprehensive datasets. However, in the real world, it is difficult to obtain the true transmittance and atmospheric light maps and to collect a large number of pairs of real sand-dust and corresponding sand-dust-free images of various outdoor scenes.

III. Proposed Method

This section describes the proposed adaptive dynamic brightness correction algorithm, frame detail enhancement based on a rolling guidance filter combined with guided image filtering, and dual-threshold interframe detection strategy.

A. ADBC algorithm for brightness enhancement

Low-light sand-dust videos are characterized by color deviations and insufficient brightness. Compared with histograms of high-quality images, the color range of each color channel of a low-light sand-dust image is narrow and concentrated on the left side of the histogram. The V component distribution of the HSV color space is concentrated in the range of low brightness values, as shown in Fig. 2. The proposed method applies color stretching and brightness correction techniques to solve these problems.

To promptly solve the color cast problem of low-light sand-dust videos, Equation (1) [35] is used to preprocess the video frames by stretching the color range.

$$\mathrm{C_{out}} = (\mathrm{C_{in}} - \mathrm{L})/(\mathrm{H} - \mathrm{L}) \times \text{ range } + \mathrm{c_{min}} \tag{1}$$

where C_{out} is the output tonal value of a pixel, C_{in} is the original tonal value of a pixel, H and L are thresholds, $range$ is the output tonal range (with a default value of 255), and C_{min} is the lowest tonal value of the pixels (with a default value of 0).

When processing low-light sand-dust videos, the brightness distribution of different frames is different. Thus, if the same brightness adjustment range is used, the brightness correction effect of certain frames may not be satisfactory. To improve the brightness of low-light sand-dust videos and dynamically determine the brightness adjustment range of each frame according to its brightness information, Equation (2) is used to process the low-light sand-dust video based on dynamic brightness correction according to the Weber–Fechner law [36].

$$F_v' = F_v \times \frac{\left(\text{ range } + k \times \overline{F_v}\right)}{\max\left(F_v, F_{v\_g}\right) + k \times \overline{F_v}} \tag{2}$$

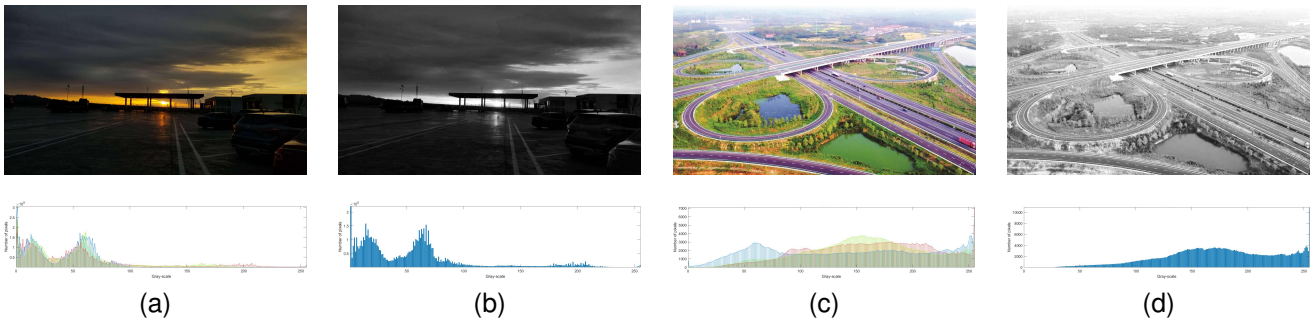

Fig. 2. Comparison of histograms of low-light sand-dust images and high-quality images. (a) Original low-light sand-dust image and its R, G, and B color channel histograms. (b) V component of the original low-light sand-dust image HSV color space and its histogram. (c) Original high-quality image and its R, G, and B color channel histograms. (d) V component of the original high-quality image HSV color space and its histogram.

where $range$ is the output brightness value range, with a default value of 255. F_v is the V component of the original video frame HSV color space, F'_v is the V component of the video frame after brightness enhancement, k is the adjustment factor, and $\overline{F_v}$ is the mean value of the V component. A smaller value of $k \times \overline{F_v}$ corresponds to a wider brightness adjustment range. For a given k, a smaller $\overline{F_v}$ corresponds to a wider range of brightness adjustment. F_{v_g} is the illumination component estimated according to F_v. Fig. 3 shows the adjusted result of the V component and its histogram for different k. As k decreases, the V component of the image becomes more concentrated in the range of high brightness values, and the details of the image are covered by high brightness.

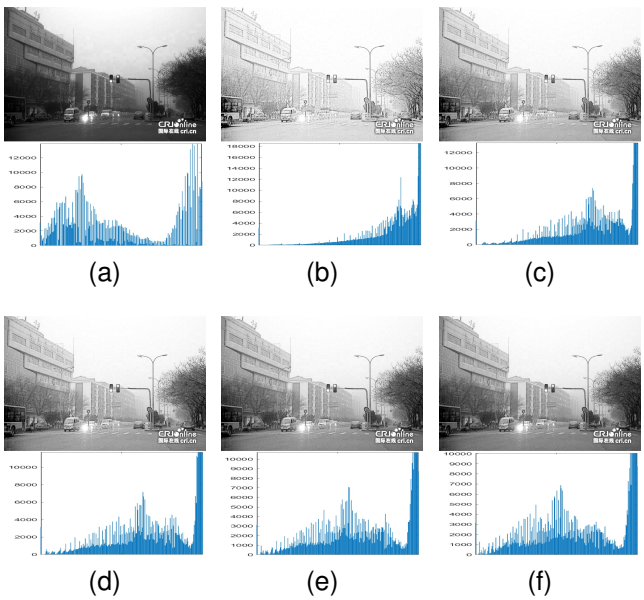

Fig. 3. Adjusted results of the V component and its corresponding histogram for different k values. (a) V component of the original image HSV color space; (b)–(f) adjusted results of the V component for $k = 0.1$, $k = 0.3$, $k = 0.5$, $k = 0.7$, and $k = 0.9$, respectively.

The multiscale Gaussian filter method is selected to extract the illumination component of the frame as it can accurately and rapidly estimate the illumination component of the scene [37]. The mathematical expression of the Gaussian function is as follows:

$$f_G(I, \sigma_s) = \frac{1}{K_p} \sum_{q \in N(p)} \exp\left(-\frac{\|p-q\|^2}{2\sigma_s^2}\right) I(q) \quad (3)$$

where σ_s is a scale parameter. $K_p = \sum_{q \in N(p)} \exp\left(-\frac{\|p-q\|^2}{2\sigma_s^2}\right)$ is used to normalize all weights of the Gaussian filter. p and q represent the coordinates of different pixel points of the image. $I(q)$ indicates the brightness value of the pixel. $N(p)$ is the domain pixel set of pixel point p, and it contains all the points in the square with point p as the center and a side length of $(2 * \sigma_s + 1)$. Using the Gaussian function to convolve the V component of the image, the estimat of the illumination component can be obtained. The output can be defined as follows:

$$F_{v\_g} = f_G(F_v, \sigma_s) \quad (4)$$

Generally, Gaussian functions with large-scale parameters can preserve the color information of the image illumination component, but the local contrast and object shape information of the image is lost. In contrast, Gaussian functions with small-scale parameters can preserve the details of the image illumination component, but they may induce halos and color artifacts, as shown in Fig. 4. To balance the global and local characteristics of the extracted illumination component, a multiscale Gaussian function is employed to extract the illumination component of the scene. Weights are assigned to the functions to obtain the estimated values of the illumination component. Such a function can be expressed as follows:

$$F_{v\_g} = \sum_{i=1}^{M} w_i \left[f_G(F_v, \sigma_{si})\right] \quad (5)$$

where w_i is the weight coefficient of the illumination component extracted by the Gaussian function with scale i, and M is the number of scales. We assume that the extracted illumination components at each scale contribute equally to the final fusion result. If the illumination component extracted by a large scale is assigned a large weight, the local contrast and object shape information of the image will be lost, and if the illumination component extracted by a small scale is assigned a large weight, artifacts may be generated. In Fig. 4, the results of $\sigma_{s0} = 1$ and $\sigma_{s5} = 200$ are similar to those shown in Figs. 4(c) and 4(h), respectively. Considering

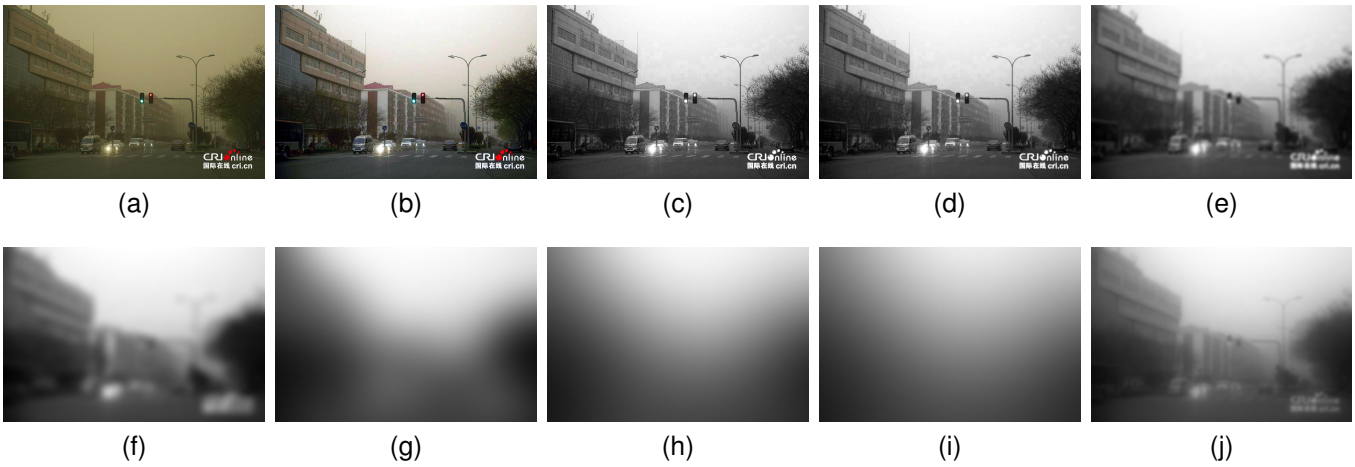

Fig. 4. Extraction of the illumination components by four-scale Gaussian filtering. (a) Original image; (b) color stretched image; (c) V component of the color stretched image; (d)–(i) illumination components obtained at $\sigma_{s0} = 1$, $\sigma_{s1} = 5$, $\sigma_{s2} = 15$, $\sigma_{s3} = 80$, $\sigma_{s4} = 150$, and $\sigma_{s5} = 200$, respectively; and (j) illumination component extracted by four-scale Gaussian filtering.

the accuracy and computational efficiency of the illumination component extraction of the image, the parameters are set as $M = 4$, $w_1 = w_2 = w_3 = w_4 = 0.25$, $\sigma_{s1} = 5$, $\sigma_{s2} = 15$, $\sigma_{s3} = 80$, and $\sigma_{s4} = 150$. The four-scale Gaussian function is used to extract the illumination component of the frame, and the result is shown in Fig. 4(j).

The adjustment factor k must be appropriately set to achieve the desired brightness correction results. As shown in Fig. 3, when $k = 0.1$, the brightness is over enhanced, and the details are masked. In comparison, when $k = 0.9$, the brightness enhancement is not adequate. To realize brightness adaptive dynamic correction and preserve the details of the image when the brightness value is changed, image fusion is performed. This process can be expressed as follows:

$$F_{fus} = \alpha_1 S_1 + \alpha_2 S_2 \tag{6}$$

where F_{fus} indicates the V component of the image after fusion, α_1 and α_2 are weight coefficients, S_1 is the V component of the original image after color stretching, and S_2 is the V component after the brightness enhancement of the image. Principal component analysis (PCA) [46] is applied to calculate α_1 and α_2 through the following steps:

1: Treat each source image S_1 and S_2 as an n-dimensional vector denoted as X_p, $p = 1, 2$.

2: Construct matrix X using the source images.

$$\mathrm{X} = [\mathrm{X}_1, \mathrm{X}_2] = \begin{bmatrix} \mathrm{X}_{11} & \mathrm{X}_{21} \\ \mathrm{X}_{12} & \mathrm{X}_{22} \\ \vdots & \vdots \\ \mathrm{X}_{1\mathrm{n}} & \mathrm{X}_{2\mathrm{n}} \end{bmatrix} \tag{7}$$

3: Determine the covariance matrix C of the data matrix X.

$$C = \begin{bmatrix} \sigma_{11}^2 & \sigma_{12}^2 \\ \sigma_{21}^2 & \sigma_{22}^2 \end{bmatrix} \tag{8}$$

where σ_{ij}^2 is the covariance of the image, which satisfies

$$\sigma_{i,j}^2 = \frac{1}{n} \sum_{l=1}^{n} \left(x_{i,l} - \bar{x}_i\right)\left(x_{j,l} - \bar{x}_j\right) \tag{9}$$

where $\bar{x}_i$ is the average brightness value of the ith source image.

4: Create the eigenvalue equation $|\lambda I - C| = 0$ and calculate the eigenvalue (λ_1, λ_2) and feature vector (ξ_1, ξ_2) of the covariance matrix C, where ξ_i is a vector $\begin{bmatrix} \xi_{\mathrm{i1}} \\ \xi_{\mathrm{i2}} \end{bmatrix}$ whose size is 2×1.

5: Select a large eigenvalue.

$$p = \operatorname{argmax}\left(\lambda_p\right), p = 1 \text{ or } 2 \tag{10}$$

6: Calculate the weight coefficient using the feature vector corresponding to the largest eigenvalue λ_p.

$$\alpha_1 = \frac{\xi_{i1}}{\xi_{i1} + \xi_{i2}} \text{ and } \alpha_2 = \frac{\xi_{i2}}{\xi_{i1} + \xi_{i2}} \tag{11}$$

where $i = p$.

7: Obtain the fused image F_{fus}.

In the PCA fusion method, image fusion is performed according to the correlation between the selected images. Data with common characteristics are compressed, and those with unique characteristics are expanded. The fusion result is shown in Fig. 5. The amount of image information gradually decreases. Thus, in the following experiments, for the two images used for image fusion, the V component of the color-stretched image and that after brightness adjustment with $k = 0.1$ are selected.

Overall, Fig. 6 illustrates the proposed process for the adaptive dynamic brightness correction of low-light sand-dust video frames.

B. RGF-GIF algorithm for detail enhancement

The details of the low-light sand-dust video frames processed by the ADBC algorithm are not adequately pronounced. These details are enhanced using a rolling guidance filter combined with guided image filtering. To promptly extract the image details, the rolling guidance filter is used to extract the structural information of the image [38].

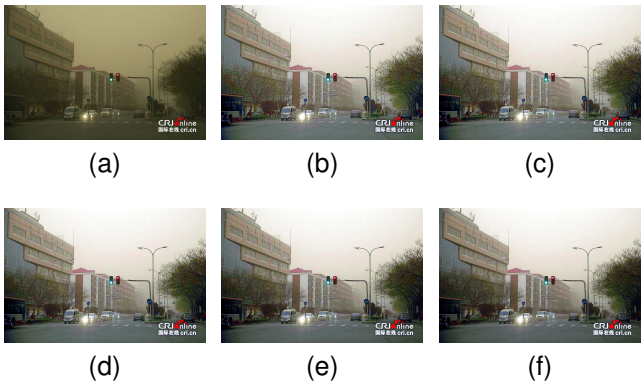

Fig. 5. Fusion results of the original image and image adjusted by different brightness correction coefficients using the PCA method. (a) Original image; (b)–(f) fusion results of the original image and brightness-corrected image for $k = 0.1$, $k = 0.3$, $k = 0.5$, $k = 0.7$, and $k = 0.9$, respectively.

The rolling guidance filter is an efficient scale-aware filter that iteratively recovers the edges of large-scale objects while smoothing small-scale objects and texture details. The implementation of the rolling guidance filter involves two steps: small-scale structure smoothing and large-scale structure edge restoration. In the first step, a Gaussian filter is used to smooth the small-scale structure of the source image. Let I be the original image and J^1 be the Gaussian smoothed image. Then, the Gaussian filtering process can be expressed as

$$J^1 = f_G\left(I, \sigma_s\right) \tag{12}$$

where the scale σ_s is used to control the window size of the Gaussian filter kernel. All structures with a scale smaller than σ_s are smoothed, but the edges of large-scale structures are blurred to a certain extent.

In the second step, bilateral filtering [47] is performed: The result J^1 of the Gaussian filter in the first step is used as the guide image, and the original image I is used to iteratively restore the smoothed large-scale structural edges. The guide image and original image of the next iteration are the output image of the previous iteration and initial original image, respectively. As the number of iterations increases, the edges of the blurred large-scale structures become clearer, and this step can be expressed as

$$J^{t+1}(p) = \frac{1}{K_p} \sum_{q \in N(p)} \exp\left(-\frac{\|p-q\|^2}{2\sigma_s^2} - \frac{\left\|U^t(p) - J^t(q)\right\|^2}{2\sigma_r^2}\right) I(q) \tag{13}$$

where $K_p = \sum_{q \in N(p)} \exp\left(-\frac{\|p-q\|^2}{2\sigma_s^2} - \frac{\left\|U^t(p) - J^t(q)\right\|^2}{2\sigma_r^2}\right)$ is used for normalization. I, which is the initial original image, is defined as in Equation (12). J^t indicates the output image of the last iteration, and t indicates the number of iterations. When $t = 0$, J^0 is a constant, and the result of Equation (13) is the same as that of Equation (12). $U^t(p)$ and $J^t(q)$ refer to the tonal values of the pixels whose coordinates are p and q in the image, respectively. σ_r is used to control the range weight. Thus, the equation of the rolling guidance filter is

$$\mathrm{O_{res}} = \mathrm{f_{rgf}}\left(\mathrm{I}, \sigma_\mathrm{s}, \sigma_\mathrm{r}, \mathrm{T}\right) \tag{14}$$

where I is the original image, O_{res} is the output image, and T is the total number of iterations.

The image details typically include the edge, corner, and other information of different objects in the image. When a rolling guidance filter is used to smooth an image, within a certain range, a higher σ_s means that more details are smoothed out. A higher σ_r means blurring of a larger amount of the target edge retained in the image. According to this principle, the difference between the original image and the image smoothed by the rolling guidance filter can be considered the image details. Therefore, the details of the image can be defined as follows:

$$\mathrm{O_d} = \mathrm{I} - \mathrm{O_{res}} \tag{15}$$

In the iterative process of the rolling guidance filter, the spatial and range weights of the filter are controlled by σ_s and σ_r, respectively. These weights facilitate the effective segmentation of different scales of the image and smoothing of the small-scale results while accurately preserving the target edge. The edge information of a part of the target increases in each iteration. As the number of iterations, T, increases, the edge information contained in O_{res} increases [38] and that of O_d decreases. In other words, the increase in T not only increases the amount of calculation but also reduces the details of O_d. Thus, we set $T = 1$. By setting the values of multiple groups of σ_s and σ_r, the details of the image shown in Fig. 5(a) are extracted. The amount of image detail information depends on the storage space occupied by the extracted detail information image. For a given resolution and format, a larger storage space occupied by the extracted detail information image corresponds to more abundant detail information extracted. The storage space can be determined by the basic attribute information of the image. When $\sigma_s = 10$ and $\sigma_r = 0.5$, the rich details of the image can be extracted, as shown in Fig. 7 and Table I.

TABLE I
THE AMOUNT OF IMAGE DETAIL INFORMATION OF FIG. 5(A) EXTRACTED WITH DIFFERENT σ_s AND σ_r. (UNIT: BYTE)

$\sigma_s = 15$	59720	59410	59397
$\sigma_s = 10$	60001	**60179**	59960
$\sigma_s = 5$	59745	60043	60043
	$\sigma_r = 0.1$	$\sigma_r = 0.5$	$\sigma_r = 0.9$

Nevertheless, O_d of the image still contains noise. Thus, when the details are directly used to enhance the details of the image processed by the ADBC algorithm, the enhanced image contains significant noise, as shown in Fig. 8(b). The guided image filter smooths the image while preserving the edges and has been widely used in noise reduction [39]. Therefore, guided image filtering is introduced to suppress the interference of noise while retaining the edge information. The image detail enhancement process can be expressed as follows:

$$\mathrm{O_e} = \mathrm{I} + \gamma \mathrm{O'_d} = \mathrm{I} + \gamma \mathrm{f_{gif(r,\varepsilon)}}\left(\mathrm{O_d}, \mathrm{O_d}\right) \tag{16}$$

where I is the image processed by the ADBC algorithm; γ is the magnification factor, with a default value of 1; $f_{gif(r,\epsilon)}$ is the GIF operator; and r and ϵ are the window radius

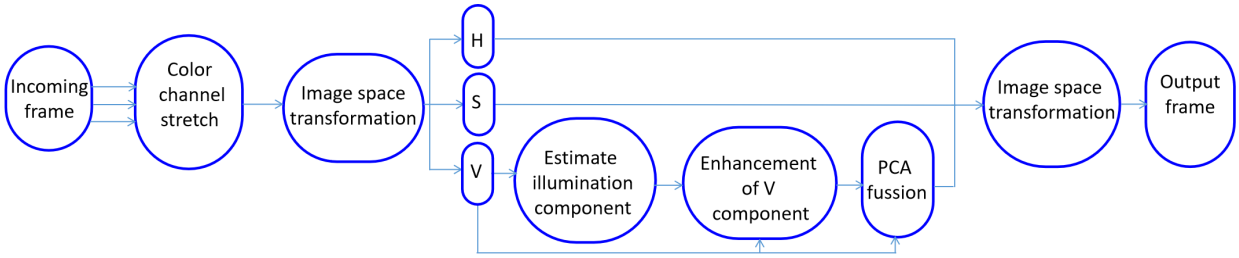

Fig. 6. The proposed process for the adaptive dynamic brightness correction of low-light sand-dust video frames.

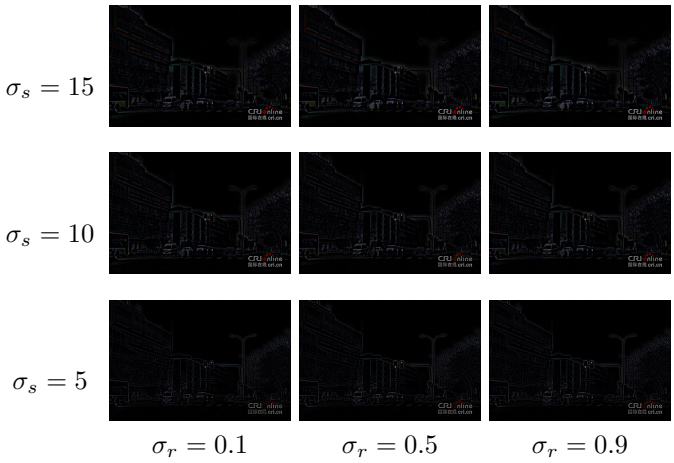

Fig. 7. Detail extraction of the image shown in Fig. 5(a) with different σ_s and σ_r. A higher σ_s means more details are smoothed out. A higher σ_r means blurring of a larger amount of the target edge retained in the image. When $\sigma_s = 10$ and $\sigma_r = 0.5$, the image details contain the maximum amount of image information.

and regularization coefficient of the GIF, set as 2 and 0.01, respectively [39].

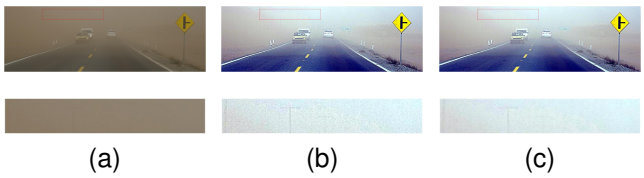

Fig. 8. The RGF-GIF algorithm can enhance the image details and suppress the noise of low-light sand-dust images. The bottom image is a magnified view of the red box. (a) Original image. (b) Image subjected to detail enhancement without guided image filtering; obvious noise can be observed on the surface. (c) Image subjected to detail enhancement with guided image filtering.

Algorithm 1 summarizes the implementation steps of the proposed RGF-GIF algorithm.

Algorithm 1 RGF-GIF algorithm for detail enhancement

Input: I, σ_s, σ_r, r, ϵ, γ
Output: O_e
1: Initialize J^0 as a constant image
2: $O_{res} \leftarrow f_{rgf}(I, \sigma_s, \sigma_r, 1)$
3: $O_d \leftarrow I - O_{res}$
4: $O'_d \leftarrow f_{gif(r,\epsilon)}(O_d, O_d)$
5: $O_e \leftarrow I + \gamma O'_d$

Compared with the detail enhancement algorithms coupled with a denoising filter, the RGF-GIF algorithm can enhance details and suppress noise while preventing the loss of image details, as shown in Fig. 9. Table II lists the quantitative evaluation indices for the RGF-GIF algorithm and its comparison algorithms used to process 200 low-light sand-dust images. With no noise-free detail-enhanced images to reference, we select the widely used reference-less image spatial quality evaluator (BRISQUE) [50], naturalness image quality evaluator (NIQE) [51], and contrast-enhanced distorted image nonreference quality evaluation index (CEIQ) [52] to quantitatively evaluate the algorithm performance. The RGF-GIF algorithm achieves the best BRISQUE and CEIQ values, and its NIQE value is second only to the method Zhang et al. [32] coupled with Kostadin et al. [49], although the image in Fig. 9(d) exhibits considerable noise amplification.

TABLE II
THE QUANTITATIVE EVALUATION INDICES FOR THE RGF-GIF ALGORITHM AND ITS COMPARISON ALGORITHMS

	Method [32]+[48]	Method [32]+[49]	Method [45]+[48]	Method [45]+[49]	RGF-GIF
BRISQUE↓	18.94	22.42	27.51	56.92	**9.42**
NIQE↓	4.29	**2.38**	4.27	4.44	2.54
CEIQ↑	3.50	3.49	3.46	3.47	**3.51**

↓ means a small metric is better, and ↑ means a large metric is better.

C. Acceleration using the dual-threshold interframe detection strategy

The adjacent frames of the video are highly similar. Thus, if the frame quality improvement method is used to process the low-light sand-dust video frame-by-frame, many repetitive calculations will be required, which will reduce the efficiency of video processing. To enhance the processing efficiency, we design a dual-threshold interframe detection strategy that uses the similarity of consecutive frames to accelerate the processing of low-light sand-dust videos. The normalized mean square error (NMSE) is used to measure the similarity between frames because it requires limited computation. The SV value between the incoming frame and buffer frame is quantitatively measured by the NMSE, which can be mathematically expressed as

$$\mathrm{SV} = 1 - \frac{1}{\mathrm{MN}} \sum_{\mathrm{m}=1}^{\mathrm{M}} \sum_{\mathrm{n}=1}^{\mathrm{N}} \frac{1}{\mathrm{L}} [\, \mathrm{F}_1(\, \mathrm{m}, \mathrm{n}) - \mathrm{F}_2(\, \mathrm{m}, \mathrm{n})]^2 \quad (17)$$

where M and N represent the total number of rows and columns of the video frame, respectively. L is the dynamic range of tonal values, and $F_1(m, n)$ and $F_2(m, n)$ represent

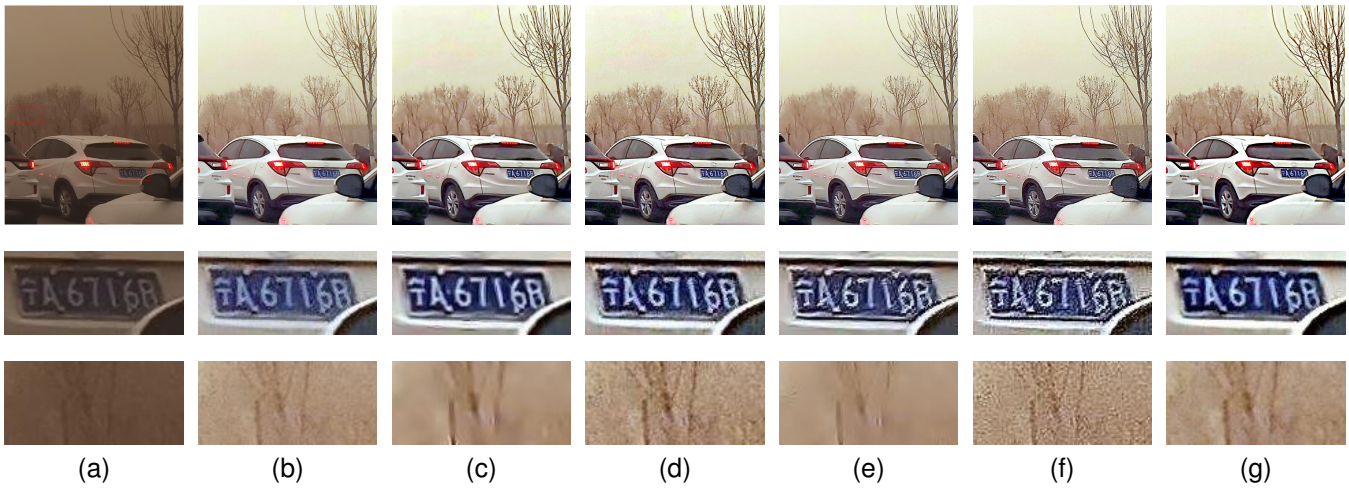

Fig. 9. Comparison of detail enhancement algorithms. (a) Original low-light sand-dust image. (b) Original image processed by the ADBC algorithm. The remaining five images show the results of detail enhancement of the image in Fig. 9(b) by the following methods: (c) Zhang et al. [32] coupled with Zhang et al. [48]; (d) Zhang et al. [32] coupled with Kostadin et al. [49]; (e) Jiang et al. [45] coupled with Zhang et al. [48]; (f) Jiang et al. [45] coupled with Kostadin et al. [49]; and (g) the proposed RGF-GIF algorithm. The noise in Figs. 9(c) and 9(e) is significantly suppressed, but certain details are lost, such as the tree branch information in the magnified area. The details in Figs. 9 (d) and 9 (f) are significantly enhanced, but the noise is not suppressed. For example, the noise of the license plate is significantly amplified. In contrast, the proposed RGF-GIF algorithm can enhance details and suppress noise while preventing the loss of image details.

the tonal values at position (m, n). F_1 and F_2 represent the incoming frame and buffer frame, respectively. The range of SV is [0,1]. A higher value means a smaller difference between frames.

In the experimental analysis, we note that several adjacent frames are almost identical. Therefore, we design the first threshold T_f for this case. When $SV \geq T_f$, we use the sum of the low-light sand-dust video frame to be processed and the frame variation associated with the frame to be processed to reduce the amount of calculation. Notably, the threshold T_f must not be set to be excessively small; otherwise, certain video frames with improved quality will have blurred edges, as shown in Fig. 10. Fig. 11 quantitatively shows the structural similarity (SSIM) between reference video 1 and the processing results of video 1 at different T_f values.

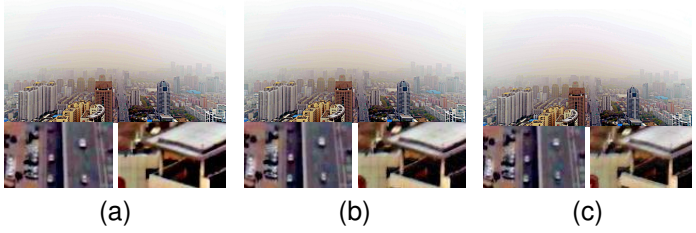

Fig. 10. Comparison results for frame 6 of Video 1 at different T_f values. The bottom images are magnified views of the red-box regions. (a) $T_f = 1$; no edge blurring occurs. (b) $T_f = 0.99$; the edges are not visually blurred. (c) $T_f = 0.97$; visible blurring occurs at the edges of buildings and moving cars. Therefore, a lower T_f corresponds to more blurring.

In addition, for a given scene, the intermediate variables are nearly unchanged when the frame quality improvement method is used to process the low-light sand-dust video frame-by-frame, as shown in Fig. 12. Therefore, we design a second threshold T_h. When $T_h \leq SV < T_f$, the intermediate

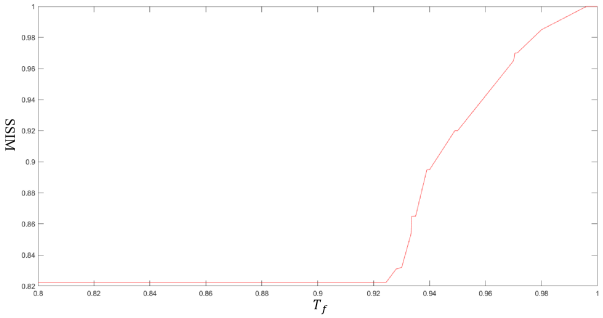

Fig. 11. Structural similarity (SSIM) between reference video 1 and the processing results of video 1 at different T_f values. Reference video 1 is the result of processing video 1 frame-by-frame using the frame quality improvement method. A lower SSIM means more severe blurring.

variables are directly substituted into Equations (1), (2), (6), and (16) to obtain the quality improvement result of the incoming frame. The threshold T_h must not be too small; otherwise, the difference between the real parameters of the incoming frame and parameters in the intermediate variables will be large, which can deteriorate the quality improvement effect of the incoming frame.

Based on this strategy, we define the speedup ratio as follows:

$$Speedup = \frac{N \times t_1}{(N-M) \times t_1 + (N-1) \times t_2 + K \times t_3 + (M-K) \times t_4} \tag{18}$$

where N represents the total number of frames of the low-light sand-dust video; t_1 represents the time required by the frame quality improvement method to improve the quality of one frame; t_2 represents the time required to calculate the SV of two frames; t_3 and t_4 denote the time required by the frame variation method and intermediate variable method to improve

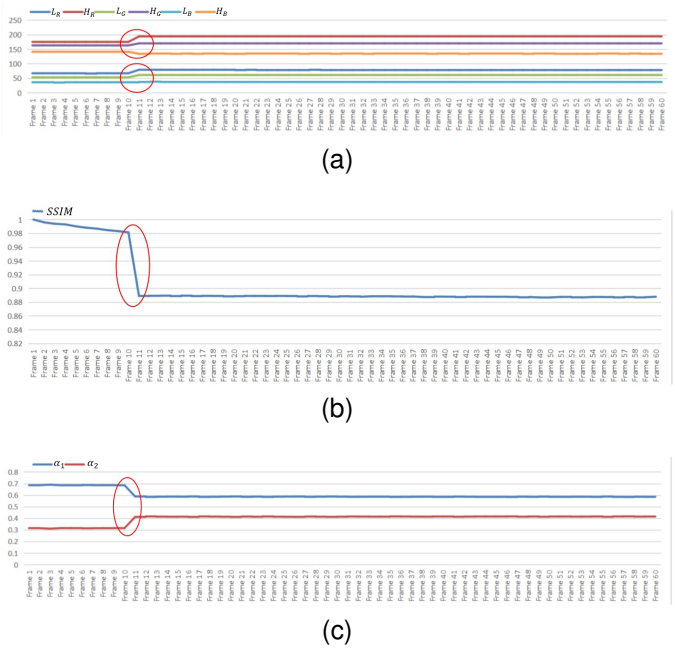

Fig. 12. Changes in intermediate variables when the frame quality improvement method is used to process low-light sand-dust video 1 frame-by-frame. In video 1, a scene change occurs between frames 10 and 11, and the intermediate variables change significantly. The intermediate variables of frames 1 to 10 and frames 11 to 60 are nearly unchanged. The SV of frames 10 and 11 is 0.926. (a) Changes in H_R, L_R, H_G, L_G, H_B, and L_B in Equation (1). (b) Changes in F_v in Equation (2). The F_v of frame 1 is used as a reference to calculate the structural similarity (SSIM) of the remaining F_v with the reference image. (c) Changes in α_1 and α_2 in Equation (6).

the quality of one frame, respectively; and M and K denote the number of frames whose quality is improved using the second method and frame variation method, respectively.

Comparing t_1, t_2, t_3 and t_4, $t_4 \approx 0.9t_1$, and t_1 is considerably larger than t_2 and t_3. Thus, we ignore $[(N-1)\times t_2 + K \times t_3]$, and Equation (18) can be rewritten as

$$Speedup = \frac{N \times t_1}{(N-M)\times t_1 + (M-K)\times 0.9t_1} = \frac{N}{N - 0.1M - 0.9K} \tag{19}$$

The proposed dual-threshold interframe detection strategy can reduce the time required for calculating the intermediate variables compared with the interframe detection strategy designed in [28].

Fig. 13 shows a comparison of the processing results obtained using the frame quality improvement method to improve the low-light sand-dust video quality frame-by-frame and those using the dual-threshold interframe detection strategy to improve the low-light sand-dust video quality.

TABLE III
THE QUANTITATIVE EVALUATION INDICES G^c, En^c, AND $\overline{r}$ IN FIGS. 13(B), 13(C), 18(B), 18(C), 19(B), AND 19(C).

	Fig. 13(b)	Fig. 13(c)	Fig. 18(b)	Fig. 18(c)	Fig. 19(b)	Fig. 19(c)
G^c	2.16	2.15	2.47	2.47	2.70	2.65
En^c	7.27	7.26	7.66	7.66	7.51	7.49
$\overline{r}$	3.92	3.75	3.79	3.78	3.44	3.30

The speedup ratio of the dual-threshold interframe detection strategy is related to the similarity of each frame of the video. A larger number of frames with similarities meeting the threshold corresponds to a higher speedup ratio.

IV. EXPERIMENTS

This section describes the experimental evaluation of the proposed method and its qualitative and quantitative comparison with state-of-the-art algorithms.

Experimental data: To evaluate the proposed method on real low-light sand-dust images and videos, we use the keywords "sand dust weather", "sandstorm", "low-light", and "night" to retrieve images and videos from the internet (baidu.com and bing.com) and create a dataset consisting of 200 images. We prepare 10 short videos using the videos recorded by surveillance equipment under sand-dust weather, among which four (videos 1–4) are full high-definition (HD) videos, four (videos 5–8) are HD videos, and two (videos 9 and 10) are standard-definition (SD) videos. The images are used to verify the effectiveness of our algorithm in improving the quality of low-light sand-dust frames, and the videos are used to verify the effectiveness of the dual-threshold interframe detection strategy in enhancing the processing efficiency of low-light sand-dust videos.

Objective evaluation indices: Given the lack of free-reference videos and images, the nonreference method is used to objectively evaluate degraded low-light sand-dust videos and images. We use three nonreference evaluation metrics to evaluate the low-light sand-dust image and video quality recovery.

1. Average gradient G^c. G^c reflects the ability of a method in expressing the details of an image and can be used to measure the relative clarity of the image [41]. An image is defined as a two-dimensional function $f(x,y)$, where (x,y) are spatial coordinates, and the amplitude f represents the intensity value (0–255) at location (x,y) in the image. G^c is formulated as

$$G^c = \frac{1}{M \times N}\sum_{i=1}^{M}\sum_{j=1}^{N}\sqrt{\frac{(\partial f/\partial x)^2 + (\partial f/\partial y)^2}{2}} \tag{20}$$

where M and N are the width and height of the image, respectively. $\partial f/\partial x$ and $\partial f/\partial y$ represent the horizontal and vertical gradients, respectively. A larger G^c corresponds to a superior recovery effect.

2. Image information entropy En^c [42]. A still image is considered an information source with a random output. Source symbol set A is defined as the set of all possible symbols $\{a_i\}$, and the probability of source symbol a_i is $P(a_i)$. Thus, the average amount of information contained in an image is

$$En^c = -\sum_{i=1}^{L} P(a_i)\log_2 P(a_i) \tag{21}$$

A larger En^c corresponds to a superior recovery effect.

3. The $\overline{r}$ measure represents the quality of contrast restoration in the sand-dust-free image [43], and its mathematical expression is

$$\overline{\mathrm{r}} = \exp\left[\frac{1}{V_r}\sum_{P_i \in \wp_r}\log(r_i)\right] \tag{22}$$

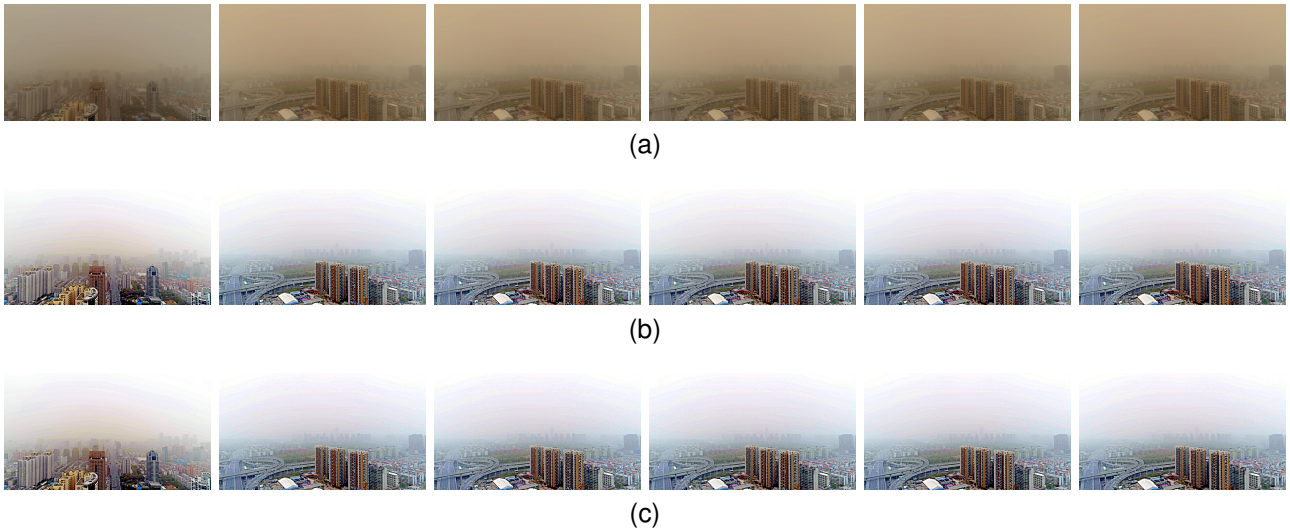

Fig. 13. Acceleration of the processing of video 1 by the dual-threshold interframe detection strategy. The thresholds T_f and T_h are set as 0.99 and 0.93, respectively. Video 1 has 60 frames, and we select frames 1, 13, 25, 37, 49, and 60 at equal intervals for presentation. (a) Original video frames. (b) Results of framewise processing using the frame quality improvement method; the processing time is 123.00 s. (c) Processing results using the dual-threshold interframe detection strategy; the processing time decreases to 34.17 s. Frame 1 in Fig. 13(b) is the same as frame 1 in Fig. 13(c). The PSNR of frame 13 in Fig. 13(b) and frame 13 in Fig. 13(c) is 75.16 dB. The PSNR of frame 25 in Fig. 13(b) and frame 25 in Fig. 13(c) is 74.09 dB. The PSNR of frame 37 in Fig. 13(b) and frame 37 in Fig. 13(c) is 73.11 dB. The PSNR of frame 49 in Fig. 13(b) and frame 49 Fig. 13(c) is 72.57 dB. The PSNR of frame 60 in Fig. 13(b) and frame 60 in Fig. 13(c) is 71.42 dB. PSNR $\geq$ 40 dB [40] corresponds to visually insensitive effects [40], and thus, the visual differences in Figs. 13(b) and 13(c) are insensitive. The differences between Figs. 13(b) and 13(c) are highlighted using quantitative evaluation indicators. As shown in Table III, compared with Fig. 13(b), the quantitative evaluation indices G^c, En^c, and $\overline{r}$ in Fig. 13(c) are 0.5%, 0.1%, and 4.3% lower, respectively. In contrast, the dual-threshold interframe detection strategy increases the processing efficiency of video 1 by 3.59 times.

where $\wp$ indicates the visible edges in the restored sand-dust image. V_r denotes the cardinal numbers of the set of visible edges in the contrast-restored image. r_i indicates the visible gradient ratio of the visible edge P_i. A larger $\overline{r}$ corresponds to a superior recovery effect.

Experimental environment: The experimental software and hardware are MATLAB R2020a. The memory is 16 GB, and unless specified otherwise, all methods are implemented using an Intel(R) Core(TM) i5-9400. The proposed can achieve real-time performance for surveillance videos using a GPU (Nvidia RTX 3080Ti).

A. Qualitative evaluation

Three low-light sand-dust images with different scenes, sizes, and degrees of influence of low light and sand dust are selected to demonstrate the effectiveness of the proposed frame quality improvement method. Eight state-of-the-art algorithms are used for comparison: [10], [12], [13], [15], [20], [28], [29], and [33].

Figs. 14 and 15 show that the images processed using the methods of (b) Li et al. [10], (d) Salazar et al. [13], (e) Cai et al. [15], and (i) He et al. [33] are dark and contain sand-dust effects. The algorithms of (f) Li et al. [20] and (h) Lei et al. [29] can improve the image brightness, but they cannot remove sand-dust. The methods of (c) Yang et al. [12] and (g) Ni et al. [28] can remove sand-dust; however, the contrast of the image processed by the method of (c) Yang et al. [12] is lower than the proposed method. Moreover, the license plate and roof in the image processed by the method of (g) Ni et al. [28] exhibit problems of color cast and noise amplification.

Fig. 16 shows that the methods of (b) Li et al. [10], (c) Yang et al. [12], (d) Salazar et al. [13], and (i) He et al. [33] produce artifacts at locations with nonuniform illumination. Although the methods of (f) Li et al. [20] and (h) Lei et al. [29] can enhance the image brightness, the images processed by the methods of (f) Li et al. [20] and (h) Lei et al. [29] have orange and pink tints, respectively. Although the approach of (g) Ni et al. [28] can remove sand-dust, the window frame has a color cast problem.

B. Quantitative evaluation

We quantitatively analyze our frame quality improvement method and eight state-of-the-art methods in terms of the average gradient G^c, image information entropy En^c, and quality $\overline{r}$ of the contrast restoration. The experimental results are summarized in Tables IV$\sim$VI. The optimal value of each evaluation index is boldfaced.

The proposed method achieves the best indices for images 1 and 3. For image 2, the proposed method achieves the highest En^c, and its visual effect is superior to that of Ni et al. [28], even though the method of Ni et al. [28] achieves the highest G^c and $\overline{r}$. To further demonstrate the advantages of our method in improving the quality of low-light sand-dust images, the mean values of the objective evaluation indices for 200 experimental images are determined, as shown in Fig. 17. The proposed frame quality improvement method outperforms the other eight methods.

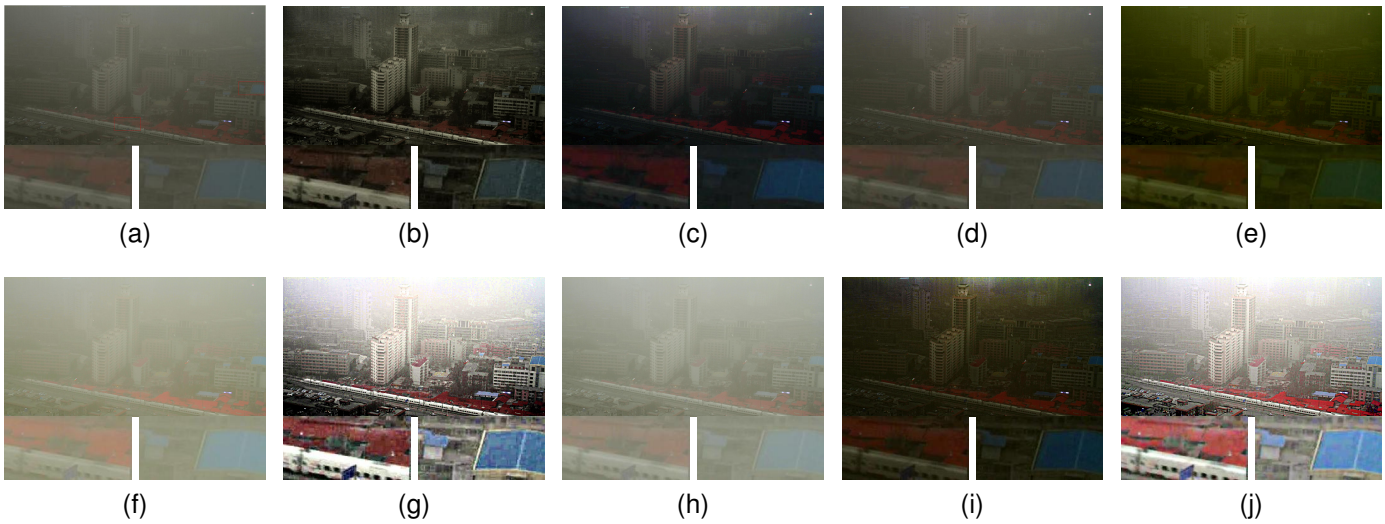

Fig. 14. Comparison results for image 1. The bottom images are magnified views of the red box regions. (a) Original image. The remaining nine images are the restoration results generated by the methods proposed by (b) Li et al. [10], (c) Yang et al. [12], (d) Salazar et al. [13], (e) Cai et al. [15], (f) Li et al. [20], (g) Ni et al. [28], (h) Lei et al. [29], (i) He et al. [33], and [j] this study.

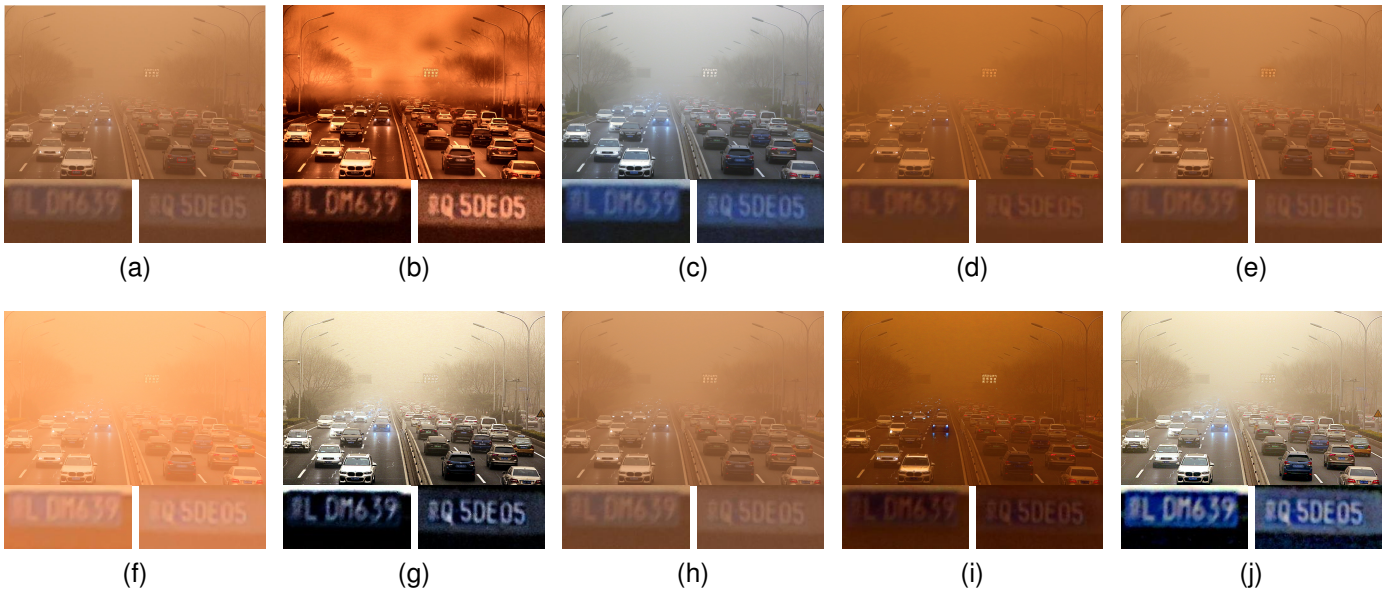

Fig. 15. Comparison results for image 2. The bottom images are magnified views of the red box regions. (a) Original image. The remaining nine images are the restoration results generated by the methods proposed by (b) Li et al. [10], (c) Yang et al. [12], (d) Salazar et al. [13], (e) Cai et al. [15], (f) Li et al. [20], (g) Ni et al. [28], (h) Lei et al. [29], (i) He et al. [33], and [j] this study.

TABLE IV
IMAGES 1∼3 RESTORATION EVALUATION BASED ON THE G^c METRIC.

	Original image	Method [10]	Method [12]	Method [13]	Method [15]	Method [20]	Method [28]	Method [29]	Method [33]	Our method
Image 1	0.44	1.64	0.64	0.51	0.52	0.40	2.38	0.46	1.18	**2.47**
Image 2	0.65	2.65	1.02	0.28	0.36	0.21	**3.46**	0.42	1.04	1.82
Image 3	0.83	3.17	1.00	0.69	0.97	0.85	3.47	1.01	1.09	**5.79**

TABLE V
IMAGES 1∼3 RESTORATION EVALUATION BASED ON THE En^c METRIC.

	Original image	Method [10]	Method [12]	Method [13]	Method [15]	Method [20]	Method [28]	Method [29]	Method [33]	Our method
Image 1	6.11	6.61	6.50	6.00	5.29	5.94	7.61	6.21	5.90	**7.69**
Image 2	6.42	7.07	7.43	5.91	6.27	5.25	7.45	6.31	6.17	**7.48**
Image 3	6.75	7.20	7.06	6.67	6.83	6.59	7.42	6.45	6.32	**7.57**

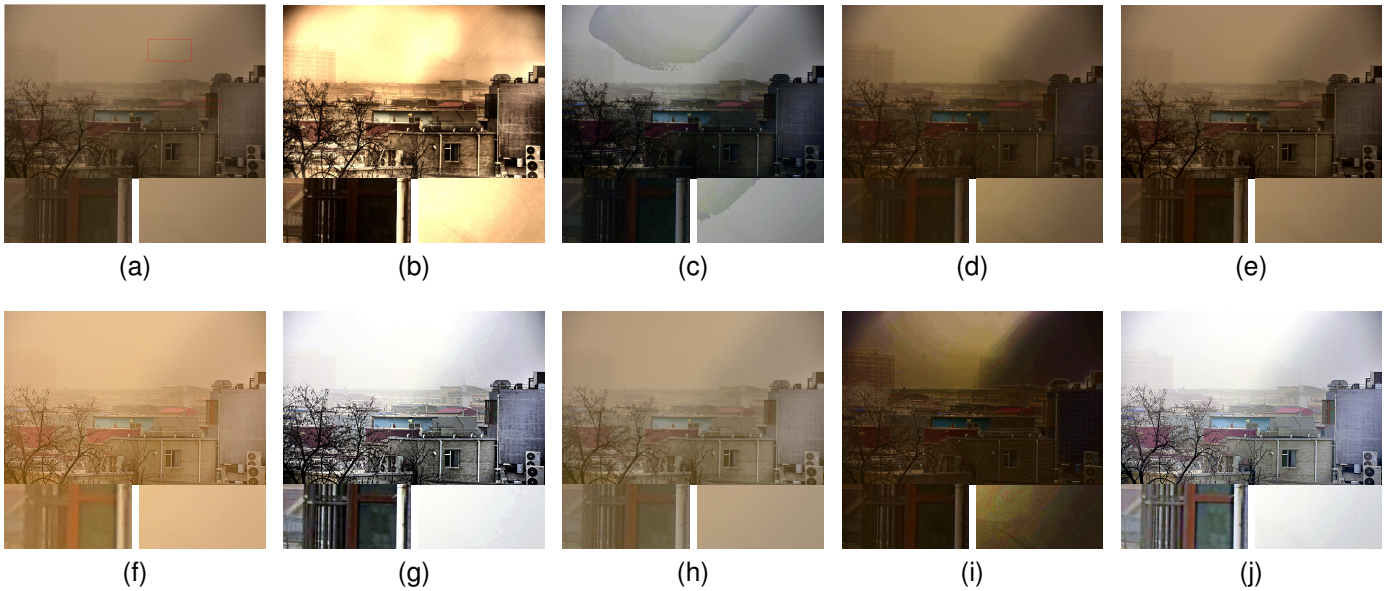

Fig. 16. Comparison results for image 3. The bottom images are magnified views of the red box regions. (a) Original image. The remaining nine images are the restoration results generated by the methods proposed by (b) Li et al. [10], (c) Yang et al. [12], (d) Salazar et al. [13], (e) Cai et al. [15], (f) Li et al. [20], (g) Ni et al. [28], (h) Lei et al. [29], (i) He et al. [33], and [j] this study.

TABLE VI
IMAGES 1∼3 RESTORATION EVALUATION BASED ON THE $\overline{r}$ METRIC.

	Method [10]	Method [12]	Method [13]	Method [15]	Method [20]	Method [28]	Method [29]	Method [33]	Our method
Image 1	3.65	1.40	1.16	1.35	6.09	6.32	1.20	2.72	**6.59**
Image 2	5.17	2.01	1.00	1.01	0.82	**7.05**	1.02	1.75	4.53
Image 3	3.86	1.02	0.82	1.16	1.83	3.78	1.14	1.81	**6.00**

TABLE VII
COMPUTATIONAL EFFICIENCY COMPARISON (UNIT: S).

	Resolution	Method [10]	Method [12]	Method [13]	Method [15]	Method [20]	Method [28]	Method [29]	Method [33]	Our method
Image 1	1996×1064	1.55	5.71	0.73	7.22	64.05	1.60	0.37	10.25	2.01
Image 2	5760×3840	16.92	58.63	7.64	52.36	980.44	15.79	4.63	86.71	19.86
Image 3	3000×2000	4.14	15.76	1.89	24.27	330.55	4.31	0.82	20.67	5.27

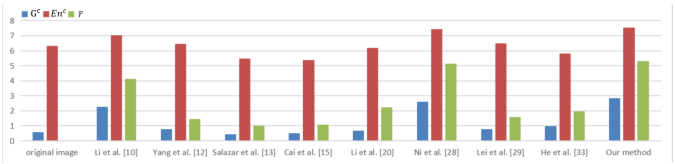

Fig. 17. Mean values of objective evaluation indices of 200 low-light sand-dust images.

C. Dual-threshold interframe detection strategy for accelerating low-light sand-dust video processing

To ensure a fair comparison of the runtime and proper implementation of the comparative algorithms, the working MATLAB codes of the eight methods are downloaded from the official/personal website of the authors or GitHub. The runtime of all the methods are listed in Table VII.

The results indicate that the proposed frame quality improvement method does not have the efficiency advantage in processing low-light sand-dust images. Using the proposed method to process video frames sequentially is time-intensive, and thus, the sand-dust videos cannot be efficiently processed. Therefore, a dual-threshold interframe detection strategy is designed to process low-light sand-dust videos. We select one full HD video, one HD video, and one SD video to demonstrate the effectiveness of the dual-threshold interframe detection strategy in efficiently processing low-light sand-dust videos. Figs. 13, 18, and 19 show the processing results of videos 1, 5, and 9 using the frame quality improvement method (frame-by-frame) and the dual-threshold interframe detection strategy. Table VIII lists the processing speeds of videos 1, 5, and 9 using the framewise processing method and dual-threshold interframe detection strategy.

The results demonstrate that the proposed dual-threshold interframe detection strategy can significantly improve the efficiency of processing low-light sand-dust videos without affecting their processing effects. In addition, we determine the average speedup ratio of the dual-threshold interframe detection strategy for all the experimental videos, as shown in Fig. 20.

The mainstream video surveillance system resolution is full HD 1920×1080, HD 1280×720, and SD 640×480. Most

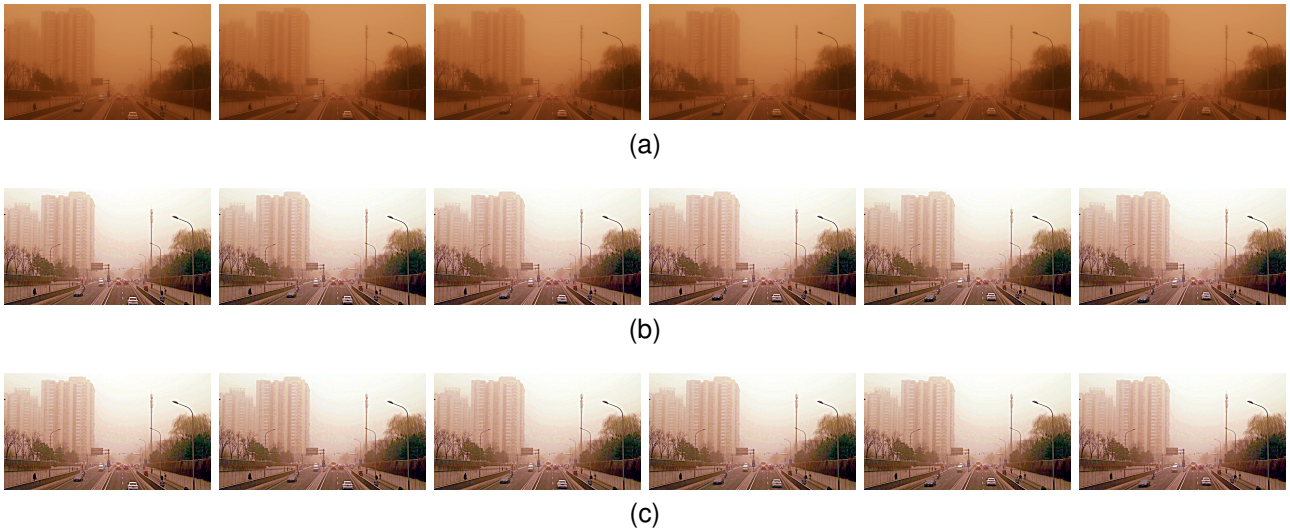

Fig. 18. Acceleration of the processing of video 5 by the dual-threshold interframe detection strategy. The thresholds T_f and T_h are set as 0.99 and 0.90, respectively. Video 5 has 24 frames, and we select frames 1, 6, 11, 16, 21, and 24 at equal intervals for presentation. (a) Original video frames. (b) Results of framewise processing using the improving frame quality method; the processing time is 22.32 s. (c) Processing results using the dual-threshold interframe detection strategy; the processing time decreases to 5.35 s. Frame 1 in Fig. 18(b) is the same as frame 1 in Fig. 18(c). The PSNR of frame 6 in Fig. 18(b) and frame 6 in Fig. 18(c) is 70.37dB. The PSNR of frame 11 in Fig. 18(b) and frame 11 in Fig. 18(c) is 70.85 dB. The PSNR of frame 16 in Fig. 18(b) and frame 16 in Fig. 18(c) is 68.15 dB. The PSNR of frame 21 in Fig. 18(b) and frame 21 in Fig. 18(c) is 67.33 dB. The PSNR of frame 24 in Fig. 18(b) and frame 24 in Fig. 18(c) is 70.40 dB. As shown in Table III, compared with Fig. 18(b), the quantitative evaluation indices G^c and En^c in Fig. 18(c) remain unchanged, and the decrease rate of the quantitative evaluation index $\overline{r}$ is 0.3%. In contrast, the dual-threshold interframe detection strategy increases the processing efficiency of video 5 by 4.16 times.

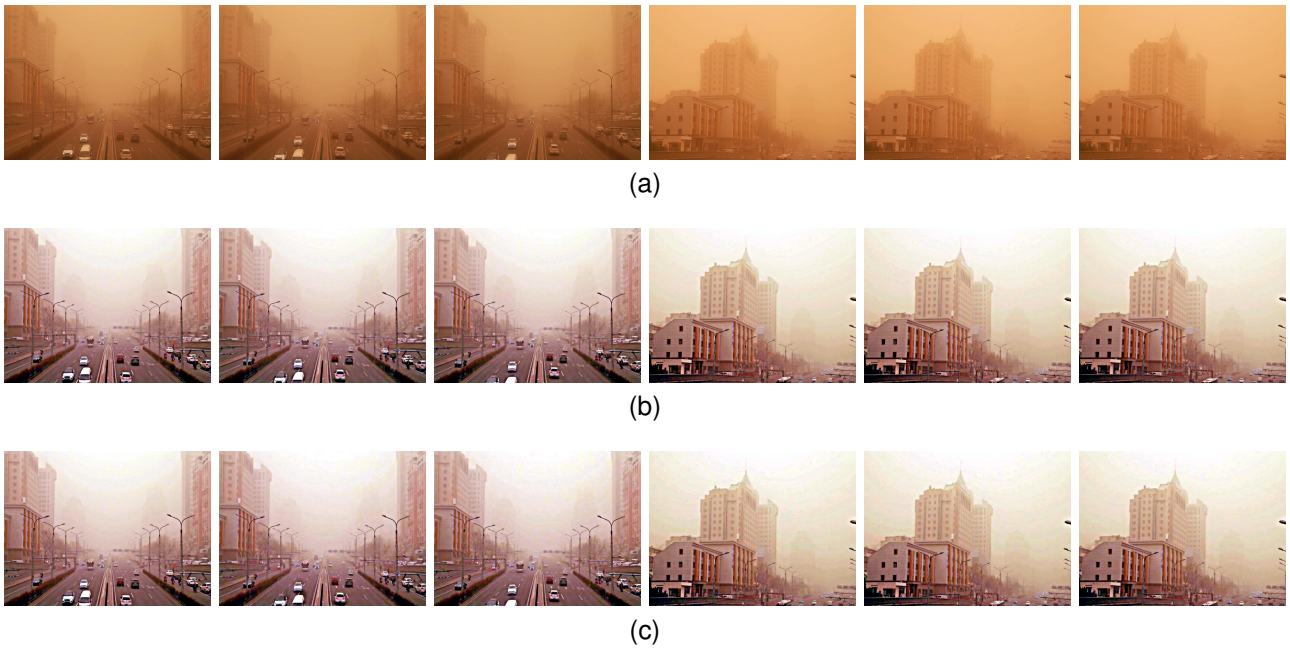

Fig. 19. Acceleration of the processing of video 9 by the dual-threshold interframe detection strategy. The thresholds T_f and T_h are set as 0.99 and 0.95, respectively. Video 9 has 30 frames, and we select frames 1, 7, 13, 19, 25, and 30 at equal intervals for presentation. (a) Original video frames. (b) Results of framewise processing using the improving frame quality method; the processing time is 11.70 s. (c) Processing results using the dual-threshold interframe detection strategy; the processing time decreases to 7.45 s. Frame 1 in Fig. 19(b) is the same as frame 1 in Fig. 19(c). The PSNR of frame 7 in Fig. 19(b) and frame 7 in Fig. 19(c) is 69.17 dB. The PSNR of frame 13 in Fig. 19(b) and frame 13 in Fig. 19(c) is 70.34 dB. The PSNR of frame 19 in Fig. 19(b) and frame 19 in Fig. 19(c) is 74.26 dB. The PSNR of frame 25 in Fig. 19(b) and frame 25 in Fig. 19(c) is 74.67 dB. The PSNR of frame 30 in Fig. 19(b) and frame 30 in Fig. 19(c) is 74.79 dB. As shown in Table III, compared with Fig. 19(b), the quantitative evaluation indices G^c, En^c, and $\overline{r}$ in Fig. 19(c) are 1.9%, 0.3%, and 4.1% lower, respectively. In contrast, the dual-threshold interframe detection strategy increases the processing efficiency of video 9 by 1.57 times.

TABLE VIII
PROCESSING SPEED COMPARISON (UNIT: FPS).

Video sequence	Resolution	Total number of frames	Processing speed of framewise method	Processing speed of framewise method (GPU)[1]	Processing speed of dual-threshold interframe detection strategy	Processing speed of dual-threshold interframe detection strategy (GPU)[1]	Speedup ratio
Video 1	1920×1080	60	0.49	6.82	1.76	24.48	3.59
Video 5	1280×720	24	1.08	9.38	4.49	39.02	4.16
Video 9	640×480	30	2.56	14.43	4.03	22.65	1.57

[1] (GPU) denotes using GPU (Nvidia RTX 3080Ti)

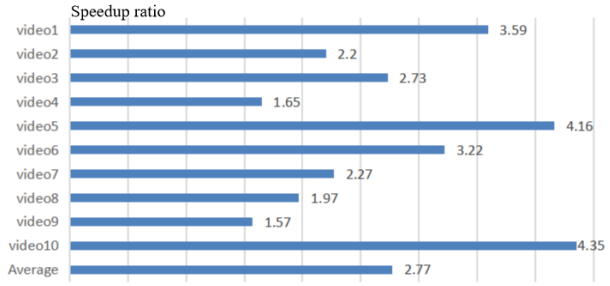

Fig. 20. Speedup ratio of the dual-threshold interframe detection strategy for all the experimental videos.

of these systems use either 15 FPS or 7.5 FPS, as higher values require a large amount of storage volume in the case of recording [44], which means that the proposed method can theoretically meet the needs of real-time processing in practical deployment.

V. CONCLUSIONS

This paper proposes an online low-light sand-dust video enhancement method using adaptive dynamic brightness correction and a rolling guidance filter. The dual-threshold interframe detection strategy adopts two strategies to process low-light sand-dust video frames. The first method has two components: an adaptive dynamic brightness correction algorithm to correct the color deviation of a low-light video frame and improve its brightness, and a rolling guidance filter combined with guided image filtering to enhance the frame details. The second method obtains the quality improvement result of the processed frame by reducing the amount of calculation. The first frame of the video is processed using the first method. The processing method of each frame after the first frame is determined according to its interframe detection value with the buffer frame. Comprehensive qualitative and quantitative experiments are performed using low-light sand-dust videos and images, and the results are compared with those of state-of-the-art methods. The results demonstrate that the proposed frame quality improvement method achieves the best visual effect in improving the quality of low-light sand-dust images along with the best objective evaluation indicators. The dual-threshold interframe detection strategy can significantly improve the efficiency of processing low-light sand-dust videos without affecting their processing effect.

ACKNOWLEDGMENTS

This work was supported by the National Science Foundation of China under Grant 62261053, the International Science and Technology Cooperation Project of the Ministry of Education of the People's Republic of China under grant 2016-2196, and the Excellent Doctoral Research Innovation Program of Xinjiang University under Grant XJU2022BS067.

REFERENCES

[1] Shen,, W., et al.: An image enhancement algorithm of video surveillance scene based on deep learning. IET Image Process. 16, 681– 690 (2022). https://doi.org/10.1049/ipr2.12286
[2] Narasimhan, S. G. , and S. K. Nayar . "Vision and the Atmosphere." International Journal of Computer Vision 48.3(2002):233-254.
[3] Z. Wang et al., "Land-Sea Target Detection and Recognition in SAR Image Based on Non-Local Channel Attention Network," in IEEE Transactions on Geoscience and Remote Sensing, vol. 60, pp. 1-16, 2022, Art no. 5237316, doi: 10.1109/TGRS.2022.3217035.
[4] Chen, Q., Zhang, A. & Pan, G. A maximum-entropy-attention-based convolutional neural network for image perception. Neural Comput & Applic (2022). https://doi.org/10.1007/s00521-022-07564-z
[5] S. Rustagi, T. Tuteja, V. Sharma, V. Gangwar and A. S. Parihar, "Comparative Study of Various Image Enhancement Techniques based on Retinex Theory and Fuzzy Logic," 2018 Second International Conference on Electronics, Communication and Aerospace Technology (ICECA), 2018, pp. 464-469, doi: 10.1109/ICECA.2018.8474787.
[6] QI, SHENGXIANG, XU, GUOJING, MOU, ZHIYING, et al. A fast-saliency method for real-time infrared small target detection[J]. Infrared physics and technology,2016,77440-450. DOI:10.1016/j.infrared.2016.06.026.
[7] J. Zhang, X. Zhou, L. Li, T. Hu and C. Fansheng, "A Combined Stripe Noise Removal and Deblurring Recovering Method for Thermal Infrared Remote Sensing Images," in IEEE Transactions on Geoscience and Remote Sensing, vol. 60, pp. 1-14, 2022, Art no. 5003214, doi: 10.1109/TGRS.2022.3196050.
[8] Shi, Z., Feng, Y., Zhao, M., Zhang, E. and He, L. (2020), Normalised gamma transformation-based contrast-limited adaptive histogram equalisation with colour correction for sand-dust image enhancement. IET Image Processing, 14: 747-756. https://doi.org/10.1049/iet-ipr.2019.0992
[9] T. H. Park and I. K. Eom, "Sand-Dust Image Enhancement Using Successive Color Balance With Coincident Chromatic Histogram," in IEEE Access, vol. 9, pp. 19749-19760, 2021, doi: 10.1109/ACCESS.2021.3054899.
[10] Z. Li, X. Zheng, B. Bhanu, S. Long, Q. Zhang and Z. Huang, "Fast Region-Adaptive Defogging and Enhancement for Outdoor Images Containing Sky," 2020 25th International Conference on Pattern Recognition (ICPR), 2021, pp. 8267-8274, doi: 10.1109/ICPR48806.2021.9412595.
[11] G. Gao, H. Lai, Z. Jia, Y. Liu and Y. Wang, "Sand-Dust Image Restoration Based on Reversing the Blue Channel Prior," in IEEE Photonics Journal, vol. 12, no. 2, pp. 1-16, April 2020, Art no. 3900216, doi: 10.1109/JPHOT.2020.2975833.
[12] YAN YANG, CHEN ZHANG, LONGLONG LIU, et al. Visibility restoration of single image captured in dust and haze weather conditions[J]. Multidimensional systems and signal processing,2020,31(2):619-633. DOI:10.1007/s11045-019-00678-z.
[13] S. Salazar-Colores, E. Cabal-Yepez, J. M. Ramos Arreguin, G. Botella, L. M. Ledesma-Carrillo and S. Ledesma, "A Fast Image Dehazing Algorithm Using Morphological Reconstruction," in IEEE Transactions on Image Processing, vol. 28, no. 5, pp. 2357-2366, May 2019, doi: 10.1109/TIP.2018.2885490.
[14] Z. Shi, Y. Feng, M. Zhao, E. Zhang and L. He, "Let You See in Sand Dust Weather: A Method Based on Halo-Reduced Dark Channel Prior Dehazing for Sand-Dust Image Enhancement," in IEEE Access, vol. 7, pp. 116722- 116733, 2019, doi: 10.1109/ACCESS.2019.2936444.

[15] B. Cai, X. Xu, K. Jia, C. Qing and D. Tao, "DehazeNet: An End-to-End System for Single Image Haze Removal," in IEEE Transactions on Image Processing, vol. 25, no. 11, pp. 5187-5198, Nov. 2016, doi: 10.1109/TIP.2016.2598681.
[16] B. Ding, H. Chen, L. Xu and R. Zhang, "Restoration of Single Sand-Dust Image Based on Style Transformation and Unsupervised Adversarial Learning," in IEEE Access, vol. 10, pp. 90092-90100, 2022, doi: 10.1109/ACCESS.2022.3200163.
[17] Liang, P., Dong, P., Wang, F. et al. Learning to remove sandstorm for image enhancement. Vis Comput (2022). https://doi.org/10.1007/s00371-022-02448-8
[18] Si, Y., Yang, F. & Liu, Z. Sand dust image visibility enhancement algorithm via fusion strategy. Sci Rep 12, 13226 (2022). https://doi.org/10.1038/s41598-022-17530-3
[19] Si, Y. , Yang, F. , Guo, Y. , Zhang, W. , & Yang, Y. . (2022). A comprehensive benchmark analysis for sand dust image reconstruction. arXiv e-prints.
[20] M. Li, J. Liu, W. Yang, X. Sun and Z. Guo, "Structure-Revealing Low-Light Image Enhancement Via Robust Retinex Model," in IEEE Transactions on Image Processing, vol. 27, no. 6, pp. 2828-2841, June 2018, doi: 10.1109/TIP.2018.2810539.
[21] K. Wei, Y. Fu, Y. Zheng and J. Yang, "Physics-Based Noise Modeling for Extreme Low-Light Photography," in IEEE Transactions on Pattern Analysis and Machine Intelligence, vol. 44, no. 11, pp. 8520-8537, 1 Nov. 2022, doi: 10.1109/TPAMI.2021.3103114.
[22] Q. Wang, L. Zhao, G. Tang, H. Zhao and X. Zhang, "Single-Image Dehazing Using Color Attenuation Prior Based on Haze-Lines," 2019 IEEE International Conference on Big Data (Big Data), 2019, pp. 5080-5087, doi: 10.1109/BigData47090.2019.9005603.
[23] P. -J. Liu, S. -J. Horng, J. -S. Lin and T. Li, "Contrast in Haze Removal: Configurable Contrast Enhancement Model Based on Dark Channel Prior," in IEEE Transactions on Image Processing, vol. 28, no. 5, pp. 2212-2227, May 2019, doi: 10.1109/TIP.2018.2823424.
[24] X. Wu, X. Liu, K. Hiramatsu and K. Kashino, "Contrast-accumulated histogram equalization for image enhancement," 2017 IEEE International Conference on Image Processing (ICIP), 2017, pp. 3190-3194, doi: 10.1109/ICIP.2017.8296871.
[25] Xuan Dong et al., "Fast efficient algorithm for enhancement of low lighting video," 2011 IEEE International Conference on Multimedia and Expo, 2011, pp. 1-6, doi: 10.1109/ICME.2011.6012107.
[26] K. Xu, X. Yang, B. Yin and R. W. H. Lau, "Learning to Restore Low-Light Images via Decomposition-and-Enhancement," 2020 IEEE/CVF Conference on Computer Vision and Pattern Recognition (CVPR), 2020, pp. 2278-2287, doi: 10.1109/CVPR42600.2020.00235.
[27] Y. Wang, R. Wan, W. Yang, H. Li, L.-P. Chau, and A. Kot, "Low-light image enhancement with normalizing flow," in Proceedings of the AAAI Conference on Artificial Intelligence, vol. 36, no. 3, 2022, pp. 2604–2612.
[28] Ni, D., Jia, Z., Yang, J. et al. A fast sand-dust video quality improvement method based on adaptive dynamic guided filtering and interframe detection strategy. J Real-Time Image Proc 19, 1181–1197 (2022). https://doi.org/10.1007/s11554-022-01248-6
[29] X. Lei, Z. Fei, W. Zhou, H. Zhou and M. Fei, "Low-light Image Enhancement Using the Cell Vibration Model," in IEEE Transactions on Multimedia, doi: 10.1109/TMM.2022.3175634.
[30] K. Srinivas, A. K. Bhandari and P. K. Kumar, "A Context-Based Image Contrast Enhancement Using Energy Equalization With Clipping Limit," in IEEE Transactions on Image Processing, vol. 30, pp. 5391-5401, 2021, doi: 10.1109/TIP.2021.3083448.
[31] Y. Gao, H. Hu, B. Li and Q. Guo, "Naturalness Preserved Nonuniform Illumination Estimation for Image Enhancement Based on Retinex," in IEEE Transactions on Multimedia, vol. 20, no. 2, pp. 335-344, Feb. 2018, doi: 10.1109/TMM.2017.2740025.
[32] Zhang Z , He H . A customized low-rank prior model for structured cartoon-texture image decomposition[J]. Signal Processing Image Communication,96(8):116308.2021,https://doi.org/10.1016/j.image.2021.
[33] K. He, J. Sun and X. Tang, "Single Image Haze Removal Using Dark Channel Prior," in IEEE Transactions on Pattern Analysis and Machine Intelligence, vol. 33, no. 12, pp. 2341-2353, Dec. 2011, doi: 10.1109/TPAMI.2010.168.
[34] LIU, JIAYING, XU, DEJIA, YANG, WENHAN, et al. Benchmarking Low-Light Image Enhancement and Beyond[J]. International Journal of Computer Vision,2021,129(4):1153-1184. DOI:10.1007/s11263-020-01418-8.
[35] S. Wang, Y. Zhang, P. Deng and F. Zhou, "Fast automatic white balancing method by color histogram stretching," 2011 4th International Congress on Image and Signal Processing, 2011, pp. 979-983, doi: 10.1109/CISP.2011.6100338.
[36] F. -Z. Ou, Y. -G. Wang, J. Li, G. Zhu and S. Kwong, "A Novel Rank Learning Based No-Reference Image Quality Assessment Method," in IEEE Transactions on Multimedia, vol. 24, pp. 4197-4211, 2022, doi: 10.1109/TMM.2021.3114551.
[37] S. -Y. Yu and H. Zhu, "Low-Illumination Image Enhancement Algorithm Based on a Physical Lighting Model," in IEEE Transactions on Circuits and Systems for Video Technology, vol. 29, no. 1, pp. 28-37, Jan. 2019, doi: 10.1109/TCSVT.2017.2763180.
[38] Q. Zhang, X. Shen, L. Xu, J. Jia, Rolling guidance filter, in:European Conference on Computer Vision, Springer, 2014, pp.815–830.
[39] K. He, J. Sun and X. Tang, "Guided Image Filtering," in IEEE Transactions on Pattern Analysis and Machine Intelligence, vol. 35, no. 6, pp. 1397-1409, June 2013, doi: 10.1109/TPAMI.2012.213.
[40] F. Porikli, "Constant time O(1) bilateral filtering," 2008 IEEE Conference on Computer Vision and Pattern Recognition, 2008, pp. 1-8, doi: 10.1109/CVPR.2008.4587843.
[41] Z. Zhu, H. Wei, G. Hu, Y. Li, G. Qi and N. Mazur, "A Novel Fast Single Image Dehazing Algorithm Based on Artificial Multiexposure Image Fusion," in IEEE Transactions on Instrumentation and Measurement, vol. 70, pp. 1-23, 2021, Art no. 5001523, doi: 10.1109/TIM.2020.3024335.
[42] J. Prakash, S. Mandal, D. Razansky and V. Ntziachristos, "Maximum Entropy Based Non-Negative Optoacoustic Tomographic Image Reconstruction," in IEEE Transactions on Biomedical Engineering, vol. 66, no.9, pp. 2604-2616, Sept. 2019, doi: 10.1109/TBME.2019.2892842.
[43] Hauti'ere, Nicolas & Tarel, Jean-Philippe & DIDIER, AUBERT & Dumont, Eric. (2008). Blind Contrast Enhancement Assessment by Gradient Ratioing at Visible Edges. Image Analysis and Stereology. 27. 10.5566/ias.v27.p87-95.
[44] Tsakanikas V , Dagiuklas T . Video surveillance systems-current status and future trends[J]. Computers & Electrical Engineering, 2017:S0045790617311813.
[45] H. Jiang, H. Cai and J. Yang, "Learning In-Place Residual Homogeneity for Image Detail Enhancement," 2018 IEEE International Conference on Acoustics, Speech and Signal Processing (ICASSP), 2018, pp. 1428-1432, doi: 10.1109/ICASSP.2018.8462182.
[46] Shlens J . A Tutorial on Principal Component Analysis[J]. International Journal of Remote Sensing, 2014, 51(2).
[47] Yang, Q., Tan, K.H., Ahuja, N.: Real-time o(1) bilateral filtering. In: IEEE Conference on Computer Vision and Pattern Recognition (CVPR). pp. 557–564 (2009)
[48] Zhang L, Bao P, Wu XL (2005) Multiscale lmmse-based image denoising with optimal wavelet selection. IEEE Trans Circuits Syst Video Technol 15(4):469–481. https://doi.org/10.1109/TCSVT.2005.844456
[49] K. Dabov, A. Foi, V. Katkovnik, K. Egiazarian, "Image denoising by sparse 3-D transform-domain collaborative filtering," IEEE Transactions on Image Processing, vol. 16, no. 8, pp. 2080–2095, Aug. 2007.
[50] A. Mittal, A. K. Moorthy and A. C. Bovik, "No-Reference Image Quality Assessment in the Spatial Domain," in IEEE Transactions on Image Processing, vol. 21, no. 12, pp. 4695-4708, Dec. 2012, doi: 10.1109/TIP.2012.2214050.
[51] A. Mittal, R. Soundararajan and A. C. Bovik, "Making a "Completely Blind" Image Quality Analyzer," in IEEE Signal Processing Letters, vol. 20, no. 3, pp. 209-212, March 2013, doi: 10.1109/LSP.2012.2227726.
[52] Y. Zhou, L. Li, H. Zhu, H. Liu, S. Wang, Y. Zhao, No-reference quality assessment for contrast-distorted images based on multifaceted statistical representation of structure, J. Vis. Commun. Image Represent. 60 (2019) 158–169.

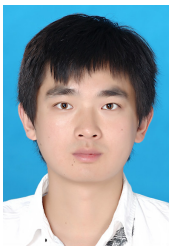

Dongdong Ni received the B.S. and M.S. degrees from the School of Information Science and Engineering, Xinjiang University, Urumqi, China, in 2011 and 2015. He is currently pursuing the Ph.D. degree from the School of Information Science and Engineering, Xinjiang University, China. His research interests include the processing of videos and images under special weather conditions.

Zhenhong Jia received the B.S. degree from Beijing Normal University, Beijing, China, in 1985, and the M.S. and Ph.D. degrees from Shanghai Jiao Tong University, Shanghai, China, in 1987 and 1995. Currently, he is a professor at the Autonomous University Key Laboratory of signal and information processing laboratory, Xinjiang University, China. His research interests include digital image processing, Photoelectric information detection and sensor.

Jie Yang received his Ph.D. degree from the Department of Computer Science, Hamburg University, Germany, in 1994. Currently, he is a professor at the Institute of Image Processing and Pattern Recognition, Shanghai Jiao Tong University, China. His major research interests include object detection and recognition, data fusion and data mining, and medical image processing.

Nikola k. Kasabov (M93SM98F10) received the M.Sc. degree in computing and electrical engineering and the Ph.D. degree in mathematical sciences from the Technical University of Sofia, Sofia, Bulgaria, in 1971 and 1975, respectively. He is the Founding Director of the Knowledge Engineering and Discovery Research Institute and a Professor of knowledge engineering with the School of Computing and Mathematical Sciences, Auckland University of Technology, Auckland, New Zealand.